SCIENCE CHINA
Physics, Mechanics & Astronomy

•Article•

April 2018 Vol. 61 No. 4: 044711
https://doi.org/10.1007/s11433-017-9127-3

Simulating coupled dynamics of a rigid-flexible multibody system and compressible fluid

Wei Hu, Qiang Tian, and HaiYan Hu*

Ministry of Education Key Laboratory of Dynamics and Control of Flight Vehicle, School of Aerospace Engineering, Beijing Institute of Technology, Beijing 100081, China

Received September 8, 2017; accepted October 25, 2017; published online February 6, 2018

As a subsequent work of previous studies of authors, a new parallel computation approach is proposed to simulate the coupled dynamics of a rigid-flexible multibody system and compressible fluid. In this approach, the smoothed particle hydrodynamics (SPH) method is used to model the compressible fluid, the natural coordinate formulation (NCF) and absolute nodal coordinate formulation (ANCF) are used to model the rigid and flexible bodies, respectively. In order to model the compressible fluid properly and efficiently via SPH method, three measures are taken as follows. The first is to use the Riemann solver to cope with the fluid compressibility, the second is to define virtual particles of SPH to model the dynamic interaction between the fluid and the multibody system, and the third is to impose the boundary conditions of periodical inflow and outflow to reduce the number of SPH particles involved in the computation process. Afterwards, a parallel computation strategy is proposed based on the graphics processing unit (GPU) to detect the neighboring SPH particles and to solve the dynamic equations of SPH particles in order to improve the computation efficiency. Meanwhile, the generalized-alpha algorithm is used to solve the dynamic equations of the multibody system. Finally, four case studies are given to validate the proposed parallel computation approach.

smoothed particle hydrodynamics (SPH), compressible flow, Riemann solver, absolute nodal coordinate formulation (ANCF), graphics processing unit (GPU)

PACS number(s): 46.70.-p, 83.50.-v, 51.35.+a

Citation: W. Hu, Q. Tian, and H. Y. Hu, Simulating coupled dynamics of a rigid-flexible multibody system and compressible fluid, Sci. China-Phys. Mech. Astron. **61**, 044711 (2018), https://doi.org/10.1007/s11433-017-9127-3

1 Introduction

Recent years have seen numerous studies on the dynamics of multibody systems, especially those on the coupled overall motion and elastic deformation of a rigid-flexible multibody system [1-3]. However, few studies have dealt with the coupled dynamics between a multibody system and surrounding fluid even though the design of many engineering products, such as the pantograph of a high speed train, the blades of a wind turbine and the inflatable membrane structures, require proper dynamic modeling and analysis of the coupling effects between the fluid and the multibody system subject to both overall motion and elastic deformation.

Over past two decades, some efforts have been made to study the aerodynamic problem of a rigid-flexible multibody system approximately. For example, Yang et al. [4] and Cai et al. [5,6] studied the dynamics of a hub-beam system subject to an overall rotation and elastic deformation in the air by using two empirical models of air drag forces [7], one is proportional to the instantaneous velocity of the beam and the other is proportional to the square of the instantaneous

*Corresponding author (email: haiyan_hu@bit.edu.cn.)

velocity of the beam. Their studies showed that the empirical models for the air drag forces enabled one to establish the coupled dynamic model of the rigid-flexible multibody system easily and the efficiency of the computation process was high since the dynamic model of the whole system was quite simple. In addition, their numerical results of the beam velocities matched well with the experimental ones. Nevertheless, their modeling of the air around the hub-beam system was so rough that there was no possibility of computing the flow field around the hub-beam system. In addition, their studies did not offer detailed theoretical analysis of the forms of the empirical models.

Recently, the dynamic studies of inflatable space structures have attracted much attention in the framework of multibody systems due to their particular features including low weight, small volume and high reliability [8-11]. However, the dynamic studies of an inflatable space structure subject to both overall motion and large deformation pose many tough problems, such as the dynamic interaction between the multibody system and the compressible fluid. Salama et al. [9] developed a Control volume (CV) method with the finite element modeling to investigate the folded inflatable cylindrical tubes. They validated their numerical simulation by using experimental results and observed a good agreement in the overall inflation dynamics. Nevertheless, their approach neglected the inertia of the inflation gas and might not be adequate for simulating the fast deployment of a flexible multibody system. Wang and Johnson [10] used the arbitrary Lagrangian and Eulerian (ALE) finite element method to model the flow of the inflation gas with the inertia force included in the dynamic equations, and predicted the gas properties at any position within the tube. This method requires a large number of ALE finite elements to model the flow of inflation gas and hence consumes much computation time. In addition, some ill-shaped finite elements may easily appear and even give rise to divergent computations.

To study the dynamics of a multibody system coupled with fluid, it is natural to integrate available numerical approaches to multibody system dynamics and to fluid dynamics. As the numerical approaches to multibody system dynamics can only be based on the Lagrangian description, the numerical approaches to fluid dynamics based on the Lagrange description become preferred candidates for the integration purpose. Among them, the smoothed particle hydrodynamics (SPH) method has shown great potentials [12-14]. As a mesh-free numerical approach, SPH method can naturally avoid many problems of grid-based methods, such as ill-shaped finite elements and time-consuming re-mesh process. In addition to the good performance in studying incompressible fluids such as liquid [15-19], the SPH method enables one to study compressible fluids such as air [20-22]. For example, Amdahl [20] firstly extended the application of the SPH method by solving a planar problem involving inviscid and compressible aerodynamic flows. His numerical results of the pressure fields and density fields showed a good agreement with the analytic results. Bohbot et al. [22] simulated the internal aerodynamics of a three-dimensional automotive combustion chamber with moving boundaries and strong variation of volume by introducing a Riemann solver into the SPH method. They also validated their numerical results via experiment data.

According to the successful applications of the SPH method to aerodynamic problems mentioned above, it is possible to study the dynamic interaction of the fluid and the flexible multibody system undergoing both overall motion and large deformation via the integration of the SPH method and the finite elements of absolute nodal coordinate formulation (ANCF) proposed by Shabana and Yakoub [23], Yakoub and Shabana [24], and Mikkola and Shabana [25] and developed by Tian et al. [26,27] and Liu et al. [28,29]. For example, the previous study of authors [30] modeled and simulated the coupled dynamics of a partially liquid-filled flexible multibody system and showed efficacy of the integrated approach of particles of SPH and finite elements of ANCF.

With the advancement of the computer hardware, new parallel computation techniques have been developed for simulating the dynamic interaction of the fluid and the multibody system by using graphics processing unit (GPU). For example, Negrut et al. [31] studied the dynamics of liquid-filled structures via a GPU based parallel algorithm in the framework of multibody system dynamics. Pazouki et al. [32] also studied the fluid-structure interactions by using a high performance computing approach based on GPU. In the previous studies of authors [30,33], the coupled dynamics of a partially liquid-filled flexible multibody system and the dynamic fracture of a flexible multibody system with initial cracks were successfully simulated via GPU.

The objective of this paper is to study the dynamic interaction of a rigid-flexible multibody system with compressible fluid via the integration of the particles of SPH for modeling the fluid, the natural coordinate formulation (NCF) [34,35] for rigid bodies and the finite elements of ANCF for soft bodies. The first problem in the above integrated approach is to cope with the compressibility of the fluid because it may lead to high oscillations of fluid density. The second problem is to establish and use the energy equation of compressible fluid because the thermodynamic temperature will not remain constant compared with previous studies under the assumption of constant temperature. The third problem is to increase the computation efficiency since the computation load for the coupled dynamic simulation is extremely high.

The remaining part of the paper is organized as follows. In sect. 2, the SPH method for aerodynamics is briefly introduced. Then in sect. 3, the boundary conditions are

outlined for periodical inflow and outflow, as well as moving bodies and fixed walls. In sect. 4, the generalized-alpha method and a two-step predictor-corrector are presented for numerical simulation, and the entire computation process is parallelized by using OpenMP and OpenACC directives. Four case studies are discussed in sect. 5 so as to validate the proposed approach. Finally, the conclusions are drawn in sect. 6.

2 SPH method for fluid dynamics

2.1 Governing equations of compressible flow

According to the SPH method [13], the computation domain of fluid can be meshed by using a number of non-connected particles. According to the continuum mechanics, the continuity equations, the momentum equations and the energy equations [13] for an arbitrary fluid particle a are written as:

$$\frac{\mathrm{d}\rho_a}{\mathrm{d}t} = -\rho_a \frac{\partial v_a^\alpha}{\partial r_a^\alpha}, \tag{1}$$

$$\frac{\mathrm{d}v_a^\alpha}{\mathrm{d}t} = \frac{1}{\rho_a}\frac{\partial \sigma_a^{\alpha\beta}}{\partial r_a^\beta}, \tag{2}$$

$$\frac{\mathrm{d}e_a}{\mathrm{d}t} = \frac{\sigma_a^{\alpha\beta}}{\rho_a}\frac{\partial v_a^\alpha}{\partial r_a^\beta}, \tag{3}$$

where ρ_a is the density of particle a, e_a is the internal energy per unit mass of particle a, r_a^β, v_a^α and $\sigma_a^{\alpha\beta}$are the entries of the position vector $\mathbf{r}_a$, the velocity vector $\mathbf{v}_a$ and the Cauchy stress tensor $\boldsymbol{\sigma}_a$ at particle a, respectively. Here, $\alpha = x, y, z$ and $\beta = x, y, z$.

The Cauchy stress tensor can be detailed as:

$$\sigma_a^{\alpha\beta} = -p_a\delta^{\alpha\beta} + \tau_a^{\alpha\beta}, \tag{4}$$

where p_a is the isotropic pressure, and $\tau_a^{\alpha\beta}$ are the entries of the shear stress $\boldsymbol{\tau}_a$. The isotropic pressure p_a in eq. (4) can be determined from the following state equation of ideal gas:

$$p_a = (\gamma - 1)\rho_a e_a, \tag{5}$$

where $\gamma = 1.4$ is the heat capacity ratio of gas. The internal energy e_a at particle a yields:

$$e_a = \frac{\kappa}{M_{\mathrm{air}}(\gamma - 1)}T_a, \tag{6}$$

where T_a is the thermodynamic temperature of particle a, $\kappa = 8.314\ \mathrm{J\ mol^{-1}\ K^{-1}}$ is a constant of ideal gas, and $M_{\mathrm{air}} = 0.02895\ \mathrm{kg/mol}$ is the molar mass of air. In addition, the speed of sound at particle a is

$$c_a = \sqrt{\gamma\frac{\partial p_a}{\partial \rho_a}} = \sqrt{\gamma(\gamma-1)e_a}. \tag{7}$$

For an arbitrary particle a in the SPH method, the field function and the corresponding gradient can be approximately expressed as:

$$\mathbf{f}(\mathbf{r}_a) = \sum_{b=1}^{N}\frac{m_b}{\rho_b}\mathbf{f}(\mathbf{r}_b)W(r_{ab}, h), \tag{8}$$

$$\nabla\cdot\mathbf{f}(\mathbf{r}_a) = \sum_{b=1}^{N}\frac{m_b}{\rho_b}\mathbf{f}(\mathbf{r}_b)\cdot\nabla_a W_{ab}, \tag{9}$$

where $\nabla_a W_{ab} = (\mathbf{r}_{ab}/r_{ab})(\partial W_{ab}/\partial r_{ab})$, $\mathbf{r}_{ab} = \mathbf{r}_a - \mathbf{r}_b$, $\mathbf{r}_a$ and $\mathbf{r}_b$ are the global position vectors of particles a and b, r_{ab} is the distance between the two particles, W_{ab} is the smoothing function between the two particles, m_b and ρ_b represent the mass and density of particle b within the support domain of particle a, h denotes the smoothing length, N is the total number of particles within the support domain of particle a, respectively. In this study, the following smoothing function [13] is used:

$$W(R,h) = \alpha_d \times\begin{cases}(3-R)^5 - 6(2-R)^5 + 15(1-R)^5, & 0\le R<1,\\ (3-R)^5 - 6(2-R)^5, & 1\le R<2,\\ (3-R)^5, & 2\le R<3,\\ 0, & R\ge 3,\end{cases} \tag{10}$$

where $R=r_{ab}/h$, α_d is called the normalization coefficient equal to $120/h$, $7/478\pi h^2$ and $3/359\pi h^3$ for one-, two-, and three-dimensional computation domain, respectively. The way of choosing the smoothing function can be found from the works by Monaghan [12] and Liu et al. [13].

Substituting eqs. (8) and (9) into the right-hand sides of eqs. (1)-(3) gives:

$$\frac{\mathrm{d}\rho_a}{\mathrm{d}t} = \sum_{b=1}^{N} m_b v_{ab}^\alpha \nabla_a^\alpha W_{ab}, \tag{11}$$

$$\frac{\mathrm{d}v_a^\alpha}{\mathrm{d}t} = -\sum_{b=1}^{N} m_b\left(\frac{p_a}{\rho_a^2} + \frac{p_b}{\rho_b^2}\right)\nabla_a^\alpha W_{ab}, \tag{12}$$

$$\frac{\mathrm{d}e_a}{\mathrm{d}t} = \frac{1}{2}\sum_{b=1}^{N} m_b\left(\frac{p_a}{\rho_a^2} + \frac{p_b}{\rho_b^2}\right)v_{ab}^\alpha\nabla_a^\alpha W_{ab}, \tag{13}$$

where $\nabla_a^\alpha W_{ab} = (r_{ab}^\alpha/r_{ab})(\partial W_{ab}/\partial r_{ab})$, v_{ab}^α are the entries of vector $\mathbf{v}_{ab} = \mathbf{v}_a - \mathbf{v}_b$. The XSPH technique [36] is used to describe the motions of the fluid particles as:

$$\frac{\mathrm{d}\mathbf{r}_a}{\mathrm{d}t} = \mathbf{v}_a - \xi\sum_{b=1}^{N}\frac{m_b}{\bar{\rho}_{ab}}\mathbf{v}_{ab}W_{ab}, \tag{14}$$

where the coefficient ξ is set as 0.5.

2.2 Riemann solver for SPH method

When the SPH method is used to model the compressible fluid, such as the air, the density and pressure of each particle may show a large difference during the computation process. In addition, two arbitrary particles cannot be located at the same position since the computation domain is discretized by particles, and the discontinuity problem will always exist between two particles [13]. Traditional SPH method can hardly deal with such a discontinuity problem and usually leads to pressure oscillations at contact interfaces between two particles.

To improve the computation accuracy of the compressible flow, a Riemann solver is used for the SPH method hereinafter. The Riemann solver was firstly formulated by Monaghan [37] and developed by Parshikov et al. [38,39], Cha and Whitworth [40] later. The main differences between the Riemann solver in SPH method and the standard solver in SPH method is the pressure and the velocity terms in the continuity equations, the momentum equations and the energy equations. The formulation is achieved by updating the pressure of particle a and particle b with the following same intermediate value:

$$\begin{cases} p_a = p_{ab}^*, \\ p_b = p_{ab}^*, \end{cases} \tag{15}$$

By using an acoustic-based solver [38], the above value in eq. (15) can be approximated as:

$$p_{ab}^* = \frac{p_b\rho_a c_a + p_a\rho_b c_b - \rho_a\rho_b c_a c_b(v_b^* - v_a^*)}{\rho_a c_a + \rho_b c_b}, \tag{16}$$

where c_a and c_b are the acoustic speeds at particles a and b. In eq. (16), the velocity projections v_a^* and v_b^* onto the line connecting the two particles can be determined as:

$$\begin{cases} v_a^* = \mathbf{v}_a \cdot \left(\dfrac{\mathbf{r}_b - \mathbf{r}_a}{r_{ba}}\right), \\ v_b^* = \mathbf{v}_b \cdot \left(\dfrac{\mathbf{r}_b - \mathbf{r}_a}{r_{ba}}\right). \end{cases} \tag{17}$$

According to the acoustic-based solver, the summation of the velocity projections should also be replaced with an intermediate value as:

$$v_a^* + v_b^* = 2v_{ab}^*, \tag{18}$$

where

$$v_{ab}^* = \frac{\rho_a c_a v_a^* + \rho_b c_b v_b^* + p_a - p_b}{\rho_a c_a + \rho_b c_b}. \tag{19}$$

Hence, substituting the intermediate values into the continuity equations gives the momentum equations and the energy equations as follows:

$$\frac{\mathrm{d}\rho_a}{\mathrm{d}t} = 2\sum_{b=1}^{N}\frac{m_b}{h}(v_{ab}^* - v_a^*)\frac{\partial W_{ab}}{\partial R}, \tag{20}$$

$$\frac{\mathrm{d}v_a^\alpha}{\mathrm{d}t} = \sum_{b=1}^{N}\frac{m_b p_{ab}^*}{h}\left(\frac{1}{\rho_a^2} + \frac{1}{\rho_b^2}\right)\frac{r_b^\alpha - r_a^\alpha}{r_{ab}}\frac{\partial W_{ab}}{\partial R}, \tag{21}$$

$$\frac{\mathrm{d}e_a}{\mathrm{d}t} = \sum_{b=1}^{N}\frac{m_b p_{ab}^*}{h}\left(\frac{1}{\rho_a^2} + \frac{1}{\rho_b^2}\right)(v_{ab}^* - v_a^*)\frac{\partial W_{ab}}{\partial R}. \tag{22}$$

It is necessary to note that, according to the work by Cha and Whitworth [40], the replacements of the pressure terms (p_a and p_b) and the velocity terms (v_a and v_b) in eqs. (11)-(13) by the intermediate values (p_{ab}^*, v_a^*, v_b^* and v_{ab}^*) in eqs. (20)-(22) do not affect the conservation of momentum and total energy.

2.3 Variable smoothing length

The smoothing length h is very important for modeling compressible flows via the SPH method because it has an influence on the efficiency of computation and the accuracy of solution directly. In the implementation of the SPH method for incompressible flows, the smoothing length is a constant depending on the initial averaged density of the system. For the problems when the fluid expands or contracts, in order to maintain consistent accuracy throughout the space, an individual smoothing length should be assigned for each particle according to the variation of the density of each particle. There are many ways to evolve the smoothing length dynamically to make sure that the number of the neighboring particles remains relatively constant. In this study, a popular method proposed by Benz [41] is adopted into the evolution of the smoothing length. The method takes the time derivative of the smoothing function in terms of the continuity equation as:

$$\frac{\mathrm{d}h_a}{\mathrm{d}t} = -\frac{1}{D}\frac{h_a}{\rho_a}\frac{\mathrm{d}\rho_a}{\mathrm{d}t}, \tag{23}$$

where the value of D is 1, 2 and 3 for one-, two-, and three-dimensional problems, respectively. Each particle has its own smoothing length since the smoothing length is assumed to vary in both time and space. However, when the smoothing length of particle a is greater than that of particle b, particle a may not be covered in the support domain of particle b although particle b is covered in the support domain of particle a. Therefore, particle b can not exert a force on particle a so that the third law of Newton's mechanics is violated. In order to preserve the reciprocal interaction between the two particles, the symmetric smoothing length should be used. As proposed by Benz [41], the following mean value of the smoothing lengths can be used for a pair of interacting particles:

$$h = \frac{h_a + h_b}{2}. \tag{24}$$

3 Boundary conditions

3.1 Boundary conditions of periodical inflow and outflow

In order to reduce the number of SPH particles involved in the computation process and improve the computation efficiency, the study adopts the boundary conditions of periodical inflow and outflow, where once a particle moves out of the outflow domain as shown in Figure 1, it moves into the inflow domain again, without any changes of the field variables. Of course, the inflow and outflow may change with each other if the direction of the flow changes. Besides the great reduction in the number of particles, the other advantage of the boundary condition of periodic inflow and outflow is that, the support domain of the particles near the boundary is not cut off all of a sudden. That is, the particles near the inflow or outflow boundary have interactions with

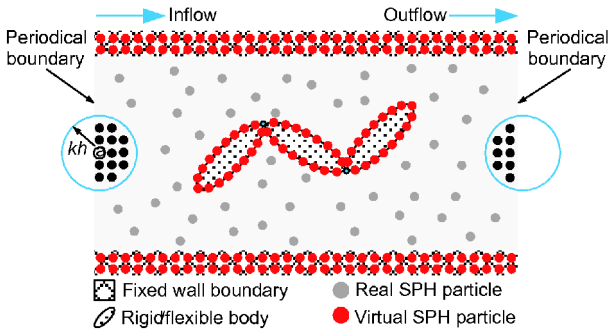

Figure 1 (Color online) General view of the boundary conditions used.

the particles near the boundary on the other side of the domain. Thus, the number of particles in their support domains is always enough. This situation is shown in Figure 1, where particle *a* lies near the left boundary and therefore its support domain extends beyond the left boundary. Under the above boundary conditions, the support domain is continued through the right boundary, and particles near the right boundary within the extended support domain have interactions with particle *a*.

3.2 Boundary conditions of moving body and fixed wall

As shown in Figure 1, some virtual SPH particles are embedded on the surface of a moving rigid/flexible body according to the previous study of authors [30,33], where the initial physical properties of virtual particles, such as the mass, density, pressure, and energy are same as those of the real particles, but the motions of the virtual particles are determined from the motion of the moving rigid/flexible body, instead of solving the dynamic equations for real particles. Hence, the position coordinates of each virtual particle are set to be those of the corresponding material point on the surface of the moving rigid/flexible body at any given moment. However, the energy and density of the virtual particles are obtained by solving the SPH equations as those of the real particles. This strategy has shown good performance in the dynamic simulation of liquid-filled flexible multibody systems in the previous work of authors [30], where detailed description about the above conditions can be found. For the virtual particles embedded in fixed wall boundaries, the only difference is to keep the position coordinates of the virtual particles unchanged.

4 Computation strategies

4.1 Solving DAEs of multibody system

The generalized coordinate vector $\mathbf{q}$ of a multibody system can be obtained by assembling the generalized coordinates of rigid bodies and the absolute nodal coordinates of finite elements of flexible bodies. In practice, the relative harder components, such as a short and thick link, in the multibody system are assumed as the rigid bodies, which can be modeled by using the NCF proposed by Javier and Eduardo [34,35]. The flexible components, such as beams and plates, are modeled by using corresponding finite elements of ANCF proposed by Gerstmayr and Shabana [42], Dmitrochenko and Pogorelov [43] and Dmitrochenko and Mikkola [44], respectively. Both NCF and ANCF give rise to constant mass matrices for rigid bodies and flexible bodies, respectively, as well as simple description for constraints. As a consequence, the dynamic equations for a constrained rigid-flexible multibody system can be expressed as a set of differential algebraic equations (DAEs) as following [1,45]:

$$\begin{cases} \mathbf{M}\ddot{\mathbf{q}} + \boldsymbol{\Phi}_q^{\mathrm{T}}\boldsymbol{\lambda} + \mathbf{F}(\mathbf{q}) - \mathbf{Q}(\mathbf{q}, \dot{\mathbf{q}}) = 0, \\ \boldsymbol{\Phi}(\mathbf{q}, t) = 0, \end{cases} \tag{25}$$

where $\mathbf{M}$ is the constant mass matrix, $\mathbf{F}(\mathbf{q})$ is the elastic force vector, $\boldsymbol{\Phi}(\mathbf{q}, t)$ represents the vector that contains all constraint equations, $\boldsymbol{\Phi}_\mathbf{q}$ is the derivative matrix of $\boldsymbol{\Phi}$ with respect to $\mathbf{q}$, $\boldsymbol{\lambda}$ is the Lagrange multiplier vector, $\mathbf{Q}(\mathbf{q}, \dot{\mathbf{q}})$is the external force vector including the interactive force applied by the fluid.

A great variety of numerical integration methods have been available for solving the DAEs like eq. (25) [46-49]. In this study, the generalized-alpha method [50,51] is used. As shown in the previous studies of authors [26,27,52,53], such an integrated method exhibits very good applicability to simulating the dynamics of rigid-flexible multibody systems with clearance joints and the dynamics of liquid-filled flexible multibody systems.

4.2 Solving ODEs of SPH particles

To simulate the fluid dynamics coupled with the rigid-flexible multibody system, a set of ordinary differential equations (ODEs), shown as eqs. (14) and (20)-(23), for the SPH particles should also be solved. A two-step predictor-corrector scheme [36,54] with second-order accuracy is adopted in the study. Detailed descriptions of this scheme can be found in refs. [30,33]. More algorithms available for solving the ODEs can be found in the work by Liu et al. [13]. For the convenience of further discussions in the following part, the left-hand sides of eqs. (14) and (20)-(23) are recast in a more compact form as following:

$$\begin{aligned} &D_a = \frac{\mathrm{d}\rho_a}{\mathrm{d}t}, \ \mathbf{F}_a = \frac{\mathrm{d}\mathbf{v}_a}{\mathrm{d}t}, \\ &A_a = \frac{\mathrm{d}e_a}{\mathrm{d}t}, \ H_a = \frac{\mathrm{d}h_a}{\mathrm{d}t}, \ \mathbf{V}_a = \frac{\mathrm{d}\mathbf{r}_a}{\mathrm{d}t}. \end{aligned} \tag{26}$$

According to the predictor-corrector scheme used in the study, the predicted values of the field variables (ρ_a, $\mathbf{v}_a$, e_a, h_a, $\mathbf{r}_a$ and p_a) at the midpoint of the current iteration step are written as:

$$\begin{cases} \overline{\rho}_a^{t+\frac{1}{2}\Delta t} = \rho_a^t + \dfrac{\Delta t}{2} D_a^t, \\ \mathbf{v}_a^{t+\frac{1}{2}\Delta t} = \mathbf{v}_a^t + \dfrac{\Delta t}{2} \mathbf{F}_a^t, \\ \overline{e}_a^{t+\frac{1}{2}\Delta t} = e_a^t + \dfrac{\Delta t}{2} A_a^t, \\ \overline{h}_a^{t+\frac{1}{2}\Delta t} = h_a^t + \dfrac{\Delta t}{2} H_a^t, \\ \overline{\mathbf{r}}_a^{t+\frac{1}{2}\Delta t} = \mathbf{r}_a^t + \dfrac{\Delta t}{2} \mathbf{V}_a^t, \\ \overline{p}_a^{t+\frac{1}{2}\Delta t} = (\gamma - 1)\overline{\rho}_a^{t+\frac{1}{2}\Delta t} \overline{e}_a^{t+\frac{1}{2}\Delta t}. \end{cases} \tag{27}$$

The updated values of the left-hand side of eq. (26) at the midpoint of the current iteration step can be easily obtained by using the predicted values shown in eq. (27). Then, the corrected results of the field variables at the midpoint of the current iteration step are further written as:

$$\begin{cases} \rho_a^{t+\frac{1}{2}\Delta t} = \rho_a^t + \dfrac{\Delta t}{2} D_a^{t+\frac{1}{2}\Delta t}, \\ \mathbf{v}_a^{t+\frac{1}{2}\Delta t} = \mathbf{v}_a^t + \dfrac{\Delta t}{2} \mathbf{F}_a^{t+\frac{1}{2}\Delta t}, \\ e_a^{t+\frac{1}{2}\Delta t} = e_a^t + \dfrac{\Delta t}{2} A_a^{t+\frac{1}{2}\Delta t}, \\ h_a^{t+\frac{1}{2}\Delta t} = h_a^t + \dfrac{\Delta t}{2} H_a^{t+\frac{1}{2}\Delta t}, \\ \mathbf{r}_a^{t+\frac{1}{2}\Delta t} = \mathbf{r}_a^t + \dfrac{\Delta t}{2} \mathbf{V}_a^{t+\frac{1}{2}\Delta t}, \\ p_a^{t+\frac{1}{2}\Delta t} = (\gamma - 1)\rho_a^{t+\frac{1}{2}\Delta t} e_a^{t+\frac{1}{2}\Delta t}. \end{cases} \tag{28}$$

According to the field variable values at the initial moment and at the midpoint of the current iteration step, the final corrected values of the field variables at the end of the current iteration step can be computed as:

$$\begin{cases} \rho_a^{t+\Delta t} = 2\rho_a^{t+\frac{1}{2}\Delta t} - \rho_a^t, \\ \mathbf{v}_a^{t+\Delta t} = 2\mathbf{v}_a^{t+\frac{1}{2}\Delta t} - \mathbf{v}_a^t, \\ e_a^{t+\Delta t} = 2e_a^{t+\frac{1}{2}\Delta t} - e_a^t, \\ h_a^{t+\Delta t} = 2h_a^{t+\frac{1}{2}\Delta t} - h_a^t, \\ \mathbf{r}_a^{t+\Delta t} = 2\mathbf{r}_a^{t+\frac{1}{2}\Delta t} - \mathbf{r}_a^t, \\ p_a^{t+\Delta t} = (\gamma - 1)\rho_a^{t+\Delta t} e_a^{t+\Delta t}. \end{cases} \tag{29}$$

4.3 Parallel computation based on OpenMP-OpenACC directives

To simulate the coupled dynamics of the fluid and the rigid-flexible multibody system, two coupled dynamic equations should be solved simultaneously. One is the ODEs for the SPH particles and the other is the DAEs for the rigid-flexible multibody system. Hence, the computation process is very time-consuming and the traditional serial computer program can hardly solve such a dynamic problem due to the high dimension of coupled nonlinear dynamics.

To increase the computation efficiency, a parallel computation approach based on OpenMP [55] and OpenACC[1)] directives is proposed as follows. The computations of the elastic force vectors and their Jacobi matrixes of the finite elements of ANCF are parallelized by using the OpenMP directives. More details of the process can be found in the works by Liu et al. [28,29] The computations of neighboring particle detections and the solution of ODEs are parallelized by using the OpenACC directives based on graphics processing unit (GPU). More details about the OpenACC based parallel scheme can be referred to the website and the previous works of authors [30,33]. All numerical simulations in the study are accomplished on a 48G RAM workstation with an Intel Xeon E5-2520*2 CPU (4 cores, 2.4GHz) and a 6G RAM NVIDIA Tesla C2070 GPU (448 cores). As well known, the OpenACC may not exhibit good performance like CUDA[2)], which enables one to get a higher speed by adjusting the data structure and the data access procedure, but OpenACC can not to do so. Theoretically speaking, hence, the maximal data transmission speed in the workstation mentioned above is 6 GB/s, but the maximal speed realized in the study is only about 2-3 GB/s. In the ongoing research, the codes will be developed in the framework of the CUDA.

In the final parallel computation program, three main modules are included. In the pre-processing module, the initial generalized coordinates of the multibody system are computed, and all constant terms are evaluated and stored in the computer memory in terms of a sparse matrix format. The initial coordinates, velocities, energies, pressures and densities of the SPH particles are computed. Initial neighboring particle detections are performed based on the domain decomposition method [30,33]. In the computation module, the ODEs of the SPH particles are firstly solved by using the predictor-corrector scheme shown in eqs. (26)-(29). Then, the accelerations and inertia forces of the virtual particles are evaluated, which can be further used as the external forces of the multibody system. The DAEs for the multibody system are solved by using generalized-alpha method. Finally, the coordinates and velocities of the virtual particles are updated according to the generalized coordinates of the multibody system. In the post-processing module, the corresponding results are stored and output, the configurations of the multibody system and the flow field are displayed. More details about the overall flowchart for the parallel computation approach are shown in Figure 2.

1) The OpenACC standard. https://www.openacc.org (accessed 8 September 2017)
2) CUDA Parallel Computing Platform. https://developer.nvidia.com/cuda-zone (accessed 8 September 2017)

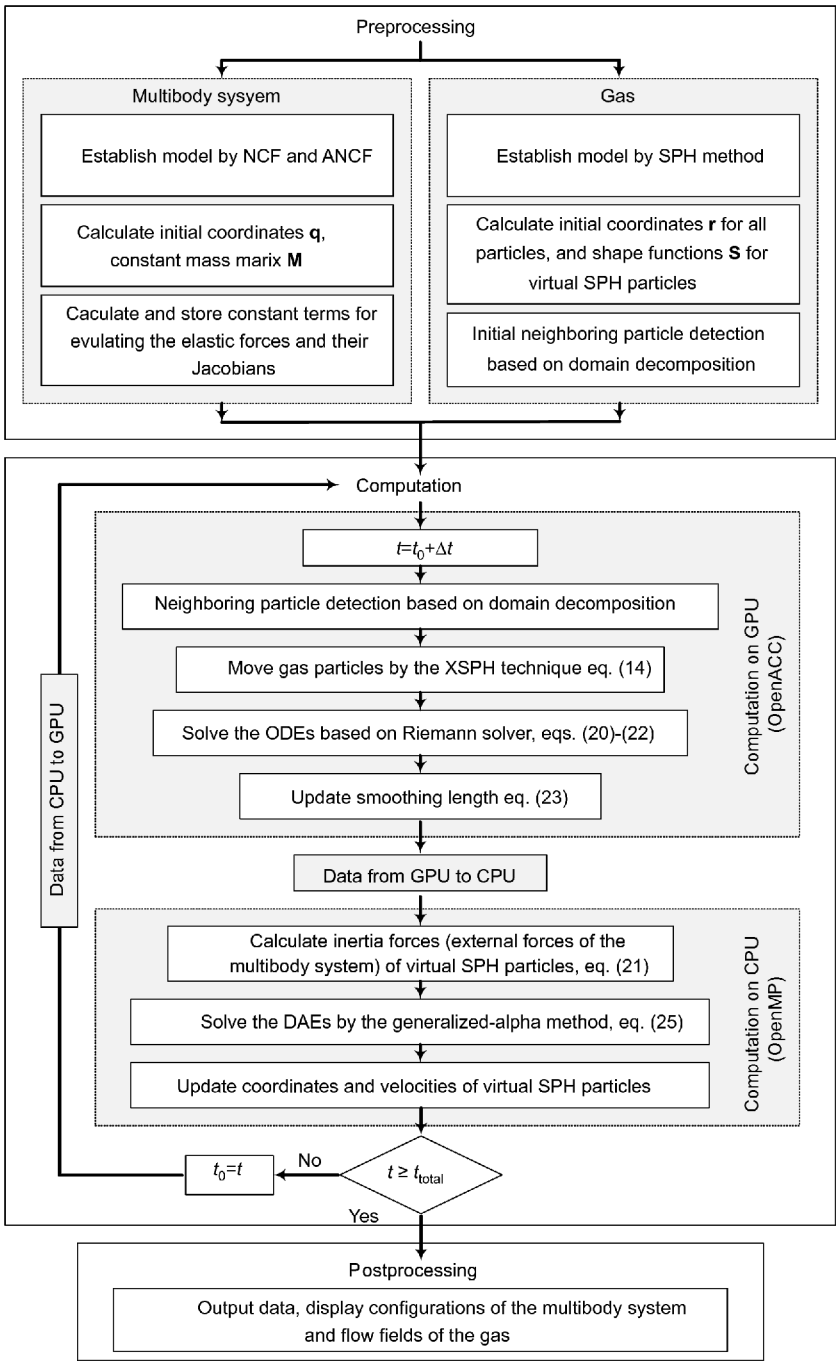

Figure 2 Flowchart of overall computation.

5 Case studies

5.1 Airflow around a circular cylinder in the pipeline

As shown in Figure 3, the first case study is to check the effectiveness of the proposed computation approach for simulating the airflow along a rigid pipeline and around a rigid circular cylinder obstacle.

Both the pipeline and the circular cylinder are fixed, and the airflow is initially static, but under the action of a constant acceleration vector $\mathbf{g} = [3, 0]^{\mathrm{T}}$ m s^{-2}. Table 1 shows the geometrical parameters of the pipeline and the circular cylinder obstacle.

In order to get quantitative results, two tracking points A and B are marked in the pipeline. The airflow is modeled by using 469567 real SPH particles and the fixed pipeline and circular cylinder obstacle are described by using 14296 virtual SPH particles. The initial particle distance is 0.1 m and the initial smoothing length is 0.125 m. Both real particles

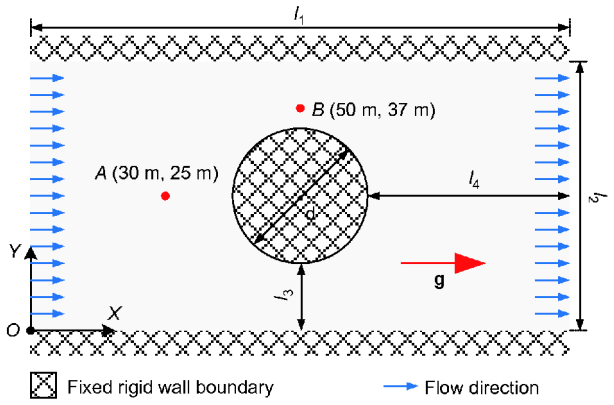

Figure 3 (Color online) Initial configuration of a pipeline with a fixed circular cylinder.

Table 1 Geometrical parameters of the pipe and the cylinder (units: m)

l_1	l_2	l_3	l_4	d
100	50	15	40	20

and virtual particles have an initial density 1.0 kg/m^3, and are subject to an initial pressure 841 Pa. The boundary conditions of periodic inflow and outflow are used as mentioned in sect. 4. The positions of virtual particles do not need to be updated, while the velocities, densities, pressures, energies and smoothing lengths will be updated as the real particles. The simulation time is 1.0 s, and the time step is chosen as 1.0×10^{-3} s according to the Courant condition and viscosity condition [56]. The CPU time used is about 15 min.

Figure 4 shows the flow fields at different moments computed by using the SPH method and the well known code FLUENT, respectively. The results are in a good agreement with each other. The subfigures clearly give the magnitude distribution of the fluid particle velocities at 4 typical moments. The maximal velocities appear on the upper and lower sides of the circular cylinder, while the minimal velocities do on the left and right sides. As shown in Figure 4, the flow field at 4 typical moments indicate that the disturbance wave generated by the circular cylinder moves away from it to the boundary of the pipeline. The wave velocity is equal to the velocity of sound obtained by eq. (7).

Figure 5 gives the time histories of the flow velocities at points A and B, which are also in a good agreement with those computed by using FLUENT.

For further verification, Figure 6 shows the pressure fields at different moments obtained by using the SPH method and FLUENT. From those numerical results, it is obvious that the computation approach proposed here is effective.

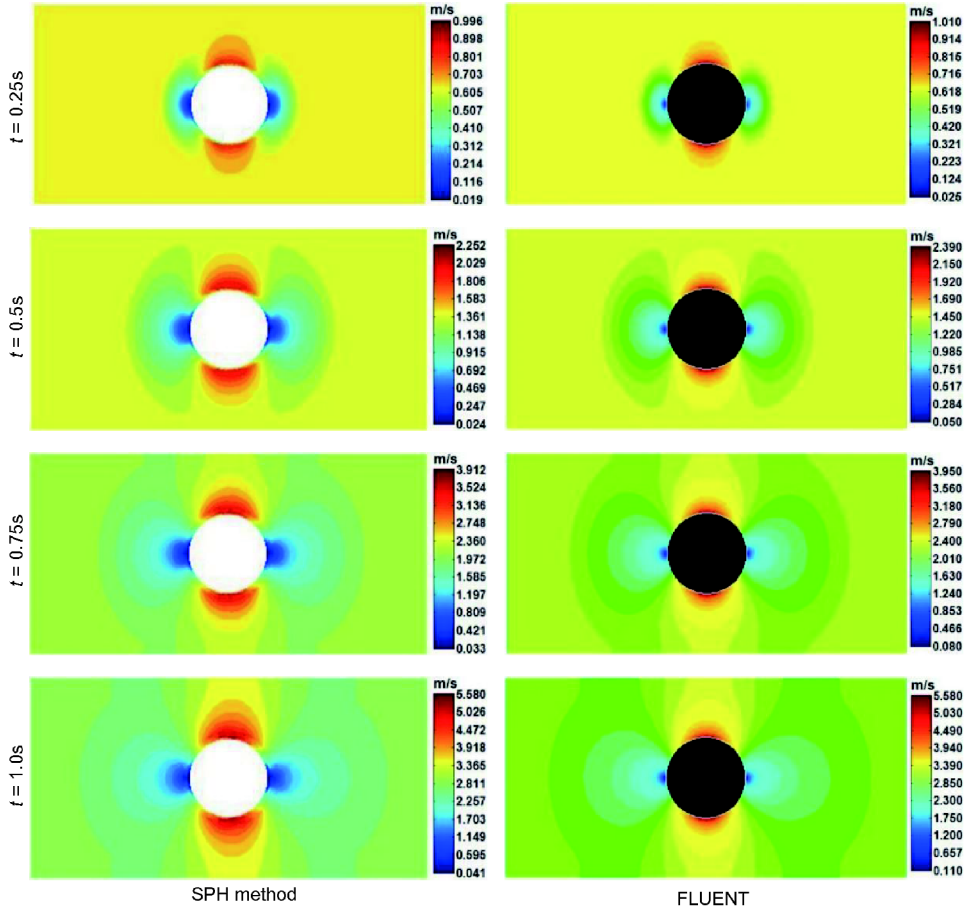

Figure 4 (Color online) The flow fields at different moments computed by using the SPH method and FLUENT.

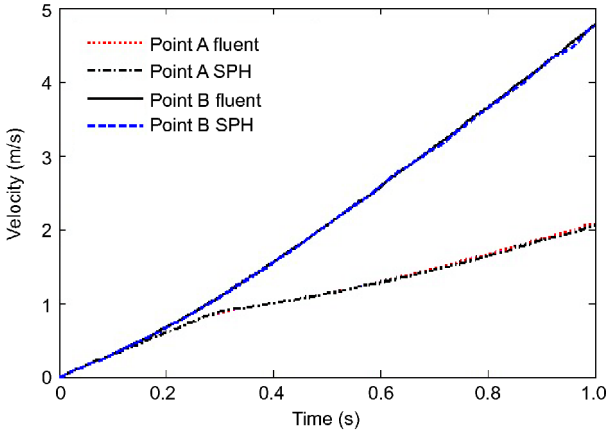

Figure 5 (Color online) Time histories of the flow velocities at points A and B computed by using the SPH method and FLUENT.

5.2 Compression of gas in a sealed rectangular cavity

This case study deals with the dynamic analysis of the gas compressed in a sealed rectangular cavity so as to validate the proposed computation approach for simulating strongly compressed flows. As shown in Figure 7, the initial configuration of the rectangular cavity has length l_1=1.0 m for each side. Under the action of an external force, the final configuration reaches length l_2=0.2 m for each side. The compression speed is set as a constant V=0.5 m/s and the directions are shown in Figure 7. With the initial particle distance 0.01 m and the initial smoothing length 0.0125 m, the final system is modeled by using 10000 real SPH particles and 2100 virtual SPH particles. Different from the first case study, the virtual particles here are not fixed. They move at a given velocity to keep a regular distribution, but the particle distance and smoothing length will decrease during the compression process. The initial pressure and initial density of all particles are 1.0×10^4 Pa and 1.293 kg/m^3. The compression time is 0.8 s, the time step is chosen as 1.0×10^{-4} s, and the total CPU time used is about 130 min. It can be observed that, with a shorter time step, the CPU time is still longer than that of the first case study, even though the number of particles is less.

Figure 8 gives the density fields of the gas computed by using the SPH method and FLUNENT at initial 4 moments. The figure indicates that the maximal density domains show a symmetrical propagation to the center under a symmetrical compression. The propagation domains reach the center at about t = 0.005 s, and the speed is about 100 m/s, which matches well with the analytical value obtained by eq. (7).

Figure 9 shows the time history of the average density in the cavity obtained by using the SPH method and the FLUENT, respectively. The two curves look almost identical

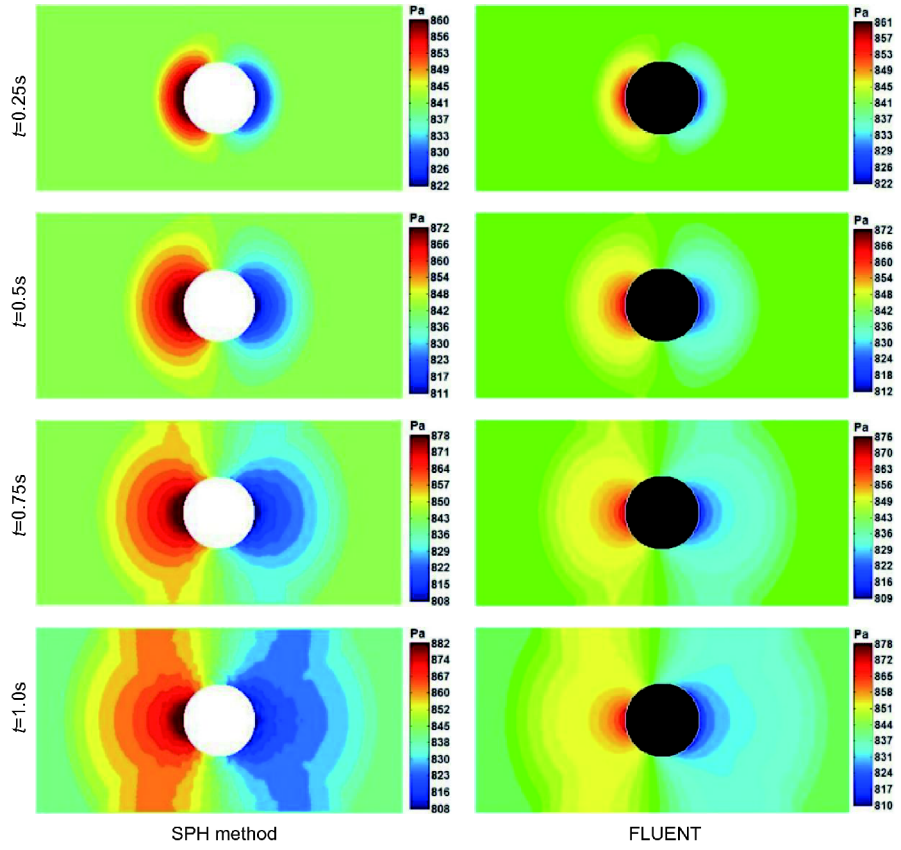

Figure 6 (Color online) The pressure fields of the airflow at different moments computed by using the SPH method and FLUENT.

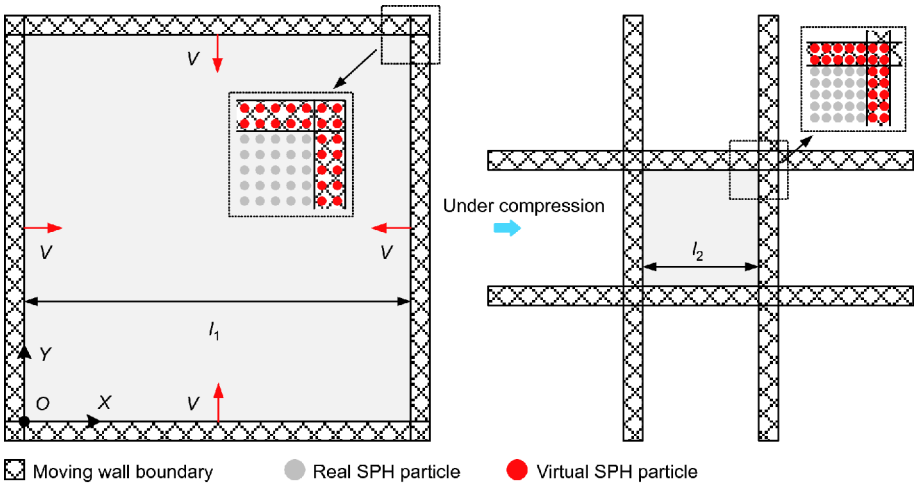

Figure 7 (Color online) Initial and final configurations of a cavity with gas compressed.

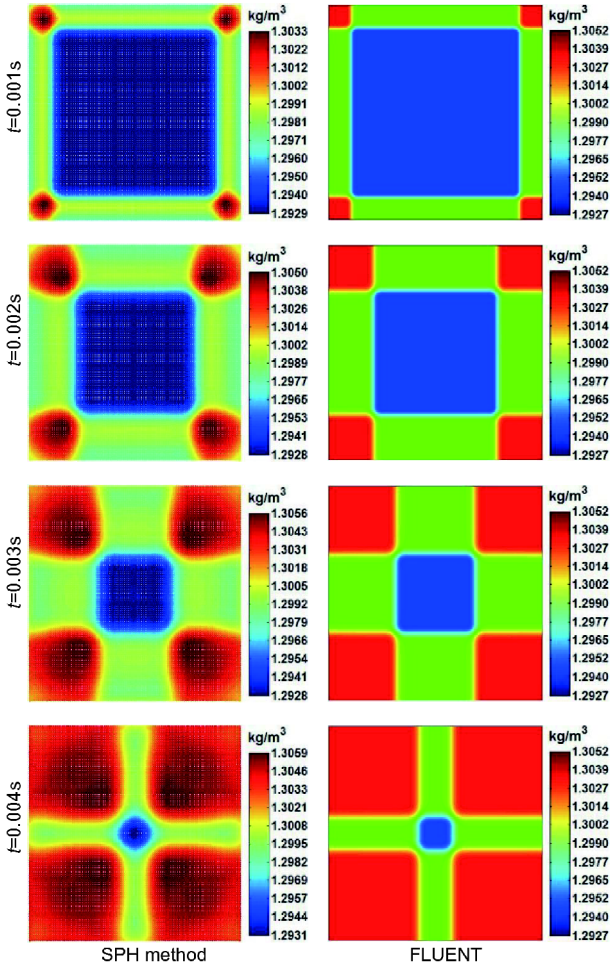

Figure 8 (Color online) The density fields of the gas at initial 4 moments computed by using the SPH method and FLUENT.

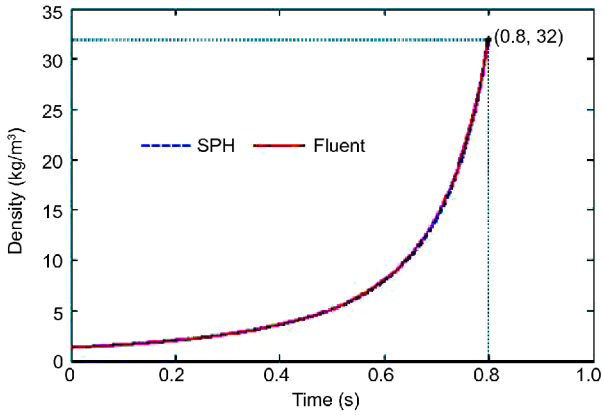

Figure 9 (Color online) Time histories of the average density in the cavity computed by using the SPH method and FLUENT.

Table 2 Work of the force and the energy increment at different moments

Time (s)	Work of the force (J)	Energy increment (J)
0.1	2219	2165
0.2	4897	4811
0.3	8240	8136
0.4	12556	12449
0.5	18379	18294
0.6	26745	26721
0.7	39966	40073
0.8	64591	64974

in Figure 9.

Table 2 gives the works done by the external force and the energy increments of the gas at different moments, which also match very well with each other. The good results show that the energy equation used in the study is effective.

As shown in Figure 10, the compression ratios are 2.041, 4.0, and 25.0, respectively, according to the size of the cavity at the moments $t = 0.3$, 0.5 and 0.8 s. Thus, the corresponding analytical values of the gas densities are 2.64, 5.17 and 32.33 kg/m^3, respectively. The simulation results of the

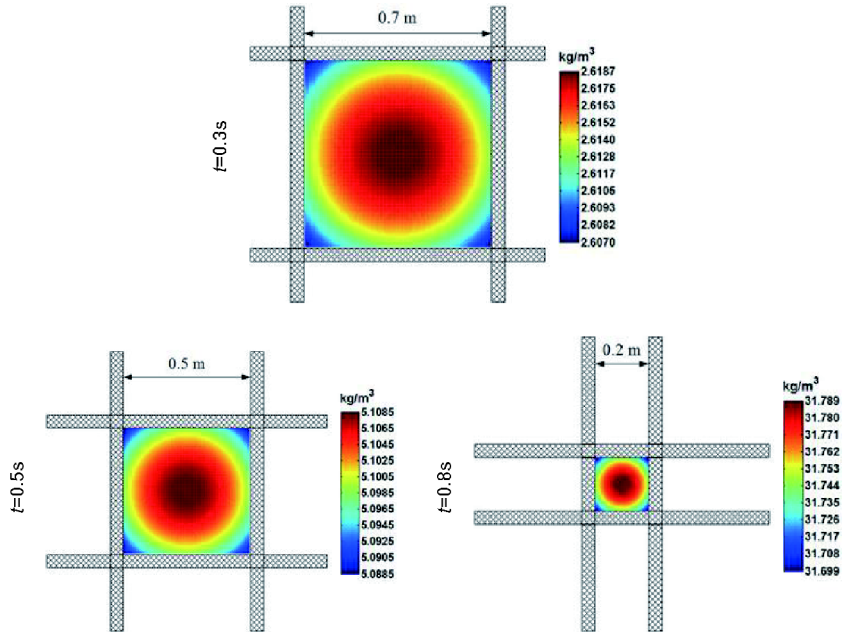

Figure 10 (Color online) The density fields of the gas at 3 typical moments computed by using the SPH method (t = 0.3 s, 0.5 s, 0.8 s).

corresponding averaged gas densities in the cavity obtained by using the SPH method are 2.61, 5.09 and 31.75 kg/m^3, respectively. The above comparisons between the analytical solution and the numerical results well support the efficacy of the computation approach developed here.

5.3 Aerodynamics of a sliding multibody system

The third case study is to check the validity of the proposed approach to simulating the aerodynamics of a rigid-flexible multibody system composed of a rigid double-pendulum sliding on a flexible cable in the air as shown in Figure 11. The sliding multibody system has been studied by Seo et al. [57], but the aerodynamic effects have not taken into consideration. As shown in Figure 11, the cable is hanging on points O and P under the action of gravity, and the gravitational acceleration vector is chosen as $\mathbf{g} = [0, -9.81]^{\mathrm{T}}$ m/s^2. The rigid double-pendulum, which has a horizontal body AB and a vertical body BC, is initial set as shown in Figure 11. The initial position of point A is equal to the position of point P.

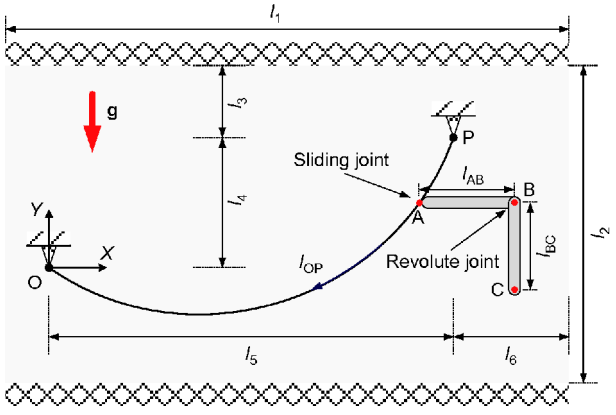

Figure 11 (Color online) Initial configuration of the sliding multibody system.

Under the action of gravity, the double-pendulum is sliding along the cable in the air. The details of the sliding multibody system can be referred to the works by Seo et al. [57]. In order to reduce the number of particles involved in the simulation, only a rectangular domain around the multibody system is modeled by using SPH particles. The upper and lower boundaries are treated as fixed boundaries, and the left and right boundaries are treated as periodical inflow and outflow. Detailed geometrical parameters of the system are shown in Table 3.

In this case, 40162 real particles and 1638 virtual particles are used to model the air, the initial particle distance and the smoothing length are 0.05 m and 0.0625 m, respectively. The initial pressure and density of the fluid particles are equal to those in the second case study. The hanging cable is modeled by using 24 cable elements of ANCF, while the double-pendulum is modeled by 2 rigid bodies of NCF. The circular radius of the cross-section of the cable is 0.0015 m. The density and the Young's modulus of the cable material are set as 5208.39 kg/m^3 and 2.0×10^5 MPa, respectively. The cross-section of the rigid bodies is set to be 0.0874 m×0.0874 m,

Table 3 Geometrical parameters of the sliding multibody system (units: m)

l_1	l_2	l_3	l_4	l_5	l_6	l_{AB}	l_{BC}	l_{OP}
10	10	3	0.5	3.8	3.5	1	1	4.02

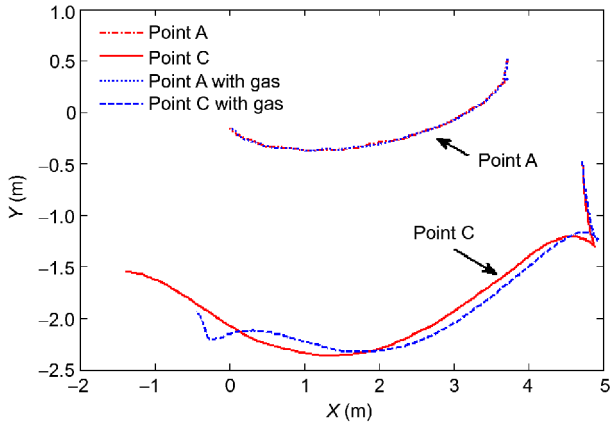

Figure 12 (Color online) Trajectories of points A and C on the double-pendulum.

and the density is 349.45 kg/m^3.

As shown in Figure 12, the two red curves are the trajectories of points A and C on the rigid double-pendulum when the aerodynamic force is ignored. They clearly indicate that the convergent results match well with those obtained by Seo et al. [57]. In addition, the two blue curves show the trajectories of the above two points when the aerodynamic force is taken into account in the dynamic simulation. The comparison of the two sets of trajectories indicates that the influence of air can not be ignored when the accurate trajectories are of concern.

Figure 13 presents the flow fields and the dynamic configurations of both sliding double-pendulum and cable at different moments, where the direction and the magnitude of the SPH particle velocities can be clearly shown. Furthermore, two fluid eddies near the two tips A and B caused by the moving double-pendulum can be clearly observed when t = 1.0 s.

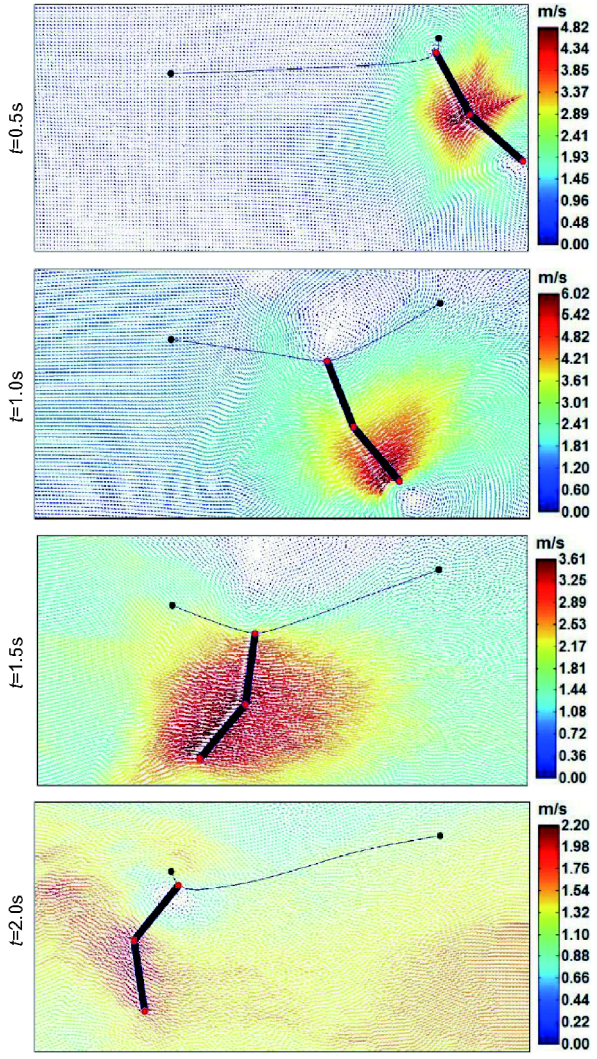

Figure 13 (Color online) The flow fields and the dynamic configurations of both sliding double-pendulum and cable at different moments.

5.4 Aerodynamics of a thin plate system

The final case study presents the three-dimensional aerodynamic analysis of a flexible multibody system composed of two square thin plates under the action of gravity vector $\mathbf{g} = [0, 0, -9.81]^T$ m/s^2 in the air. As shown in Figure 14, plate I is hinged at three equidistance points A, B and C, while plates I and II are hinged at three equidistance points D, E and F. Point P is the center on the right edge of plate II. The thickness, mass density, Young's modulus and Poisson's ratio of the material are taken to be 2.0×10^{-3} m, 1000 kg/m^3, 1.0×10^7 Pa and 0.3, respectively. Each plate is modeled by using 100 rectangular plate elements of ANCF with the same size. Similar case studies to testify the rectangular plate elements of ANCF are referred to the works [43,58].

A three-dimensional rectangular domain around the double-plate system is modeled by using SPH particles, and the size of the domain is also given in Table 4. The upper, lower,

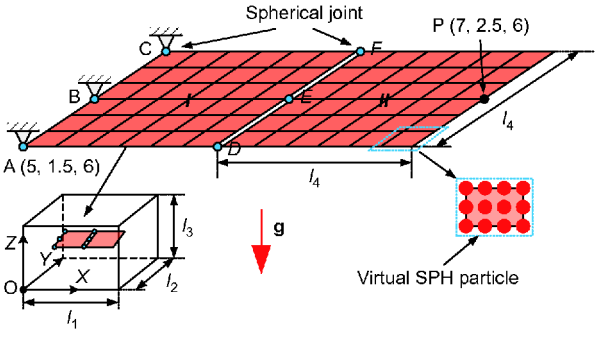

Figure 14 (Color online) Initial configuration of a double-plate system under gravity in the air.

front and back boundaries are treated as fixed boundaries, and the left and right boundaries are treated as periodical inflow and outflow.

In order to study the effects of the number of SPH particles

Table 4 Geometrical parameters of the double-plate system (units: m)

l_1	l_2	l_3	l_4
10	5	7	2

Table 5 Influence of the number of SPH particles on the computation efficiency

	Model II	Model III	Model IV
Initial particle distance (m)	0.2	0.111	0.0667
Smoothing length h (m)	0.25	0.139	0.0833
Number of real particles	46590	264294	1206570
Number of virtual particles	28210	85626	229830
Step size (s)	2.0×10^{-3}	1.0×10^{-3}	5.0×10^{-4}
Computation time (min)	91	275	1104

on the numerical simulation, three models are comparatively studied, as shown in Table 5. The table also shows the initial particle distance, smoothing length, step size, and computation time of three models. Furthermore, Model I is the case study without the aerodynamic force taken into account.

Figures 15 and 16 present the time histories of the displacements and velocities for point P in X- and Z-direction for different models, respectively. They not only show the convergent results, but also indicate that the movement of double-plate system in the air exhibits a little bit of hysteresis and smaller amplitude of the velocities under the action of the aerodynamic force.

Figure 17 shows the dynamic configurations of the double-plate system and the three-dimensional flow fields around the system at 6 typical instants. From the flow fields, the direction and magnitude of the SPH particles can be clearly observed, and the three-dimensional fluid eddies can also be observed in Figure 17 when t = 1.0 s in the flow fields.

6 Conclusions

As a continuing research of the previous studies of authors, a new computation approach is proposed to model and simulate the coupled aerodynamics of a rigid-flexible multibody system subject to both overall motion and large deformation with compressible fluid. In the proposed approach, the SPH method is used to model the fluid and a Riemann solver is introduced to cope with the flow compressibility. To deal with the coupled dynamics between the fluid and the multibody system, the virtual particles of SPH are embedded in the interface boundaries of the multibody system and the fluid. To avoid truncations of the supporting domains and reduce the number of fluid particles involved in the computation process, the boundary conditions of the periodic inflow and outflow are used in the computation process. The

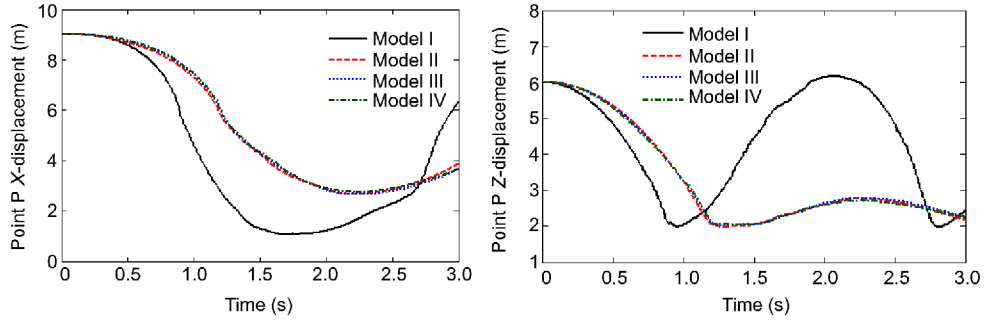

Figure 15 (Color online) Displacements of point P in X-, Z-directions computed via different models.

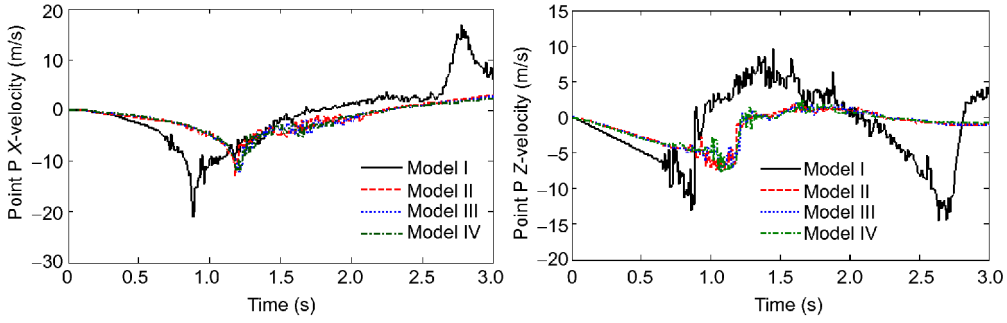

Figure 16 (Color online) Velocities of point P in X-, Z-directions computed via different models.

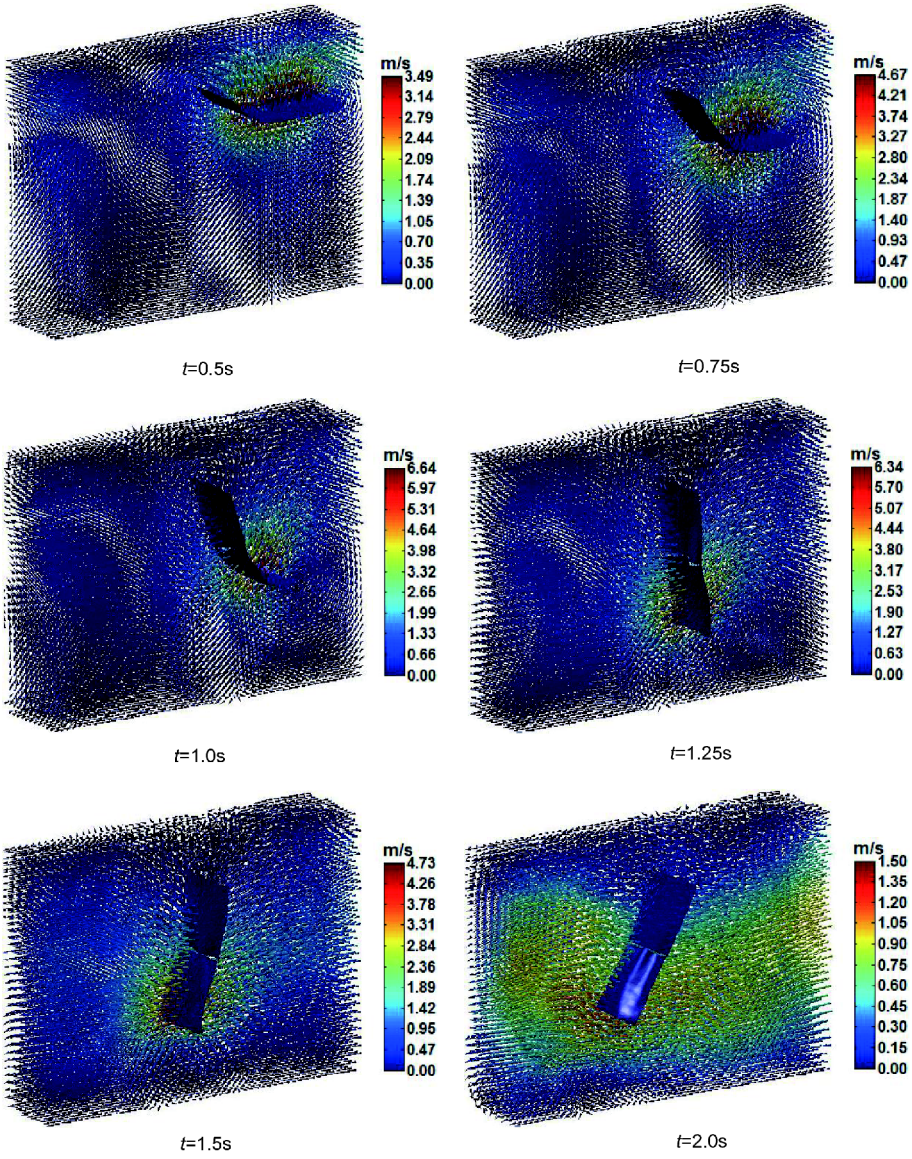

Figure 17 (Color online) Dynamic configurations of the double-plate system and flow fields at different moments.

ODEs for the SPH particles are solved by using a two-step predictor-corrector scheme with the second-order accuracy, while the DAEs for the multibody system are solved by using the generalized-alpha method. Finally, four case studies are presented to validate the effectiveness of the proposed computation approach. The numerical results indicate the potential of the proposed approach to simulate the dynamic interaction of the fluid and the rigid-flexible multibody system undergoing both overall motion and large deformation. The approach proposed is being further developed to study the aeroelastic problem of a three dimensional wing with a flapping control surface, where the flow field around the control surface exhibits very complicated phenomena.

This work was supported by the 111 China Project (Grant No. B16003) and the National Natural Science Foundation of China (Grant Nos. 11290151, 11702022, and 11221202).

1 A. A. Shabana, *Dynamics of Multibody Systems,* 3rd ed (Cambridge University Press, New York, 2005).
2 W. Schiehlen, Multibody Syst. Dyn. **18**, 3 (2007).
3 J. Gerstmayr, H. Sugiyama, and A. Mikkola, J. Comput. Nonlinear Dyn. **8**, 031016 (2013).
4 H. Yang, J. Hong, and Z. Yu, J. Sound Vib. **266**, 759 (2003).
5 G. P. Cai, J. Z. Hong, and S. X. Yang, Mech. Res. Commun. **32**, 173 (2005).
6 G. P. Cai, and C. W. Lim, J. Sound Vib. **318**, 1 (2008).
7 J. N. Juang, and L. G. Horta, J. Guid. Control Dyn. **10**, 387 (1987).
8 A. L. Clem, S. W. Smith, and J. A. Main, "A pressurized deployment model for inflatable space structures" AIAA Paper No. AIAA-2000-1808, 1999.
9 M. Salama, C. P. Kuo, and M. Lou, AIAA J. **38**, 2277 (2000).
10 J. T. Wang, and A. R. Johnson, "Deployment simulation methods for ultra-lightweight inflatable structures" NASA/TM 2003-212410, ARL-TR-2973, 2003.
11 J. Z. Wei, H. F. Tan, H. W. Sun, and X. W. Du, in *The 51st AIAA/*

ASME/ASCE/AHS/ASC Structures, Structural Dynamics, and Materials Conference, Oriando, USA, 12-15 April (2010).
12 J. J. Monaghan, Rep. Prog. Phys. **68**, 1703 (2005).
13 G. R. Liu, and M. B. Liu, *Smoothed Particle Hydrodynamics: A Meshfree Particle Method* (World Scientific, Singapore, 2003).
14 M. B. Liu, and G. R. Liu, Arch. Comput. Methods Eng. **17**, 25 (2010).
15 B. Bouscasse, A. Colagrossi, S. Marrone, and M. Antuono, J. Fluids Struct. **42**, 112 (2013).
16 A. Eghtesad, A. R. Shafiei, and M. Mahzoon, J. Fluids Struct. **30**, 141 (2012).
17 J. Grant, M. Prakash, S. E. Semercigil, and Ö. F. Turan, J. Fluids Struct. **54**, 74 (2015).
18 X. Liu, P. Lin, and S. Shao, J. Fluids Struct. **48**, 46 (2014).
19 A. Marsh, M. Prakash, E. Semercigil, and Ö. F. Turan, J. Fluids Struct. **27**, 1165 (2011).
20 D. Amdahl, "Modeling aerodynamic problems using smoothed particle hydrodynamics (SPH)", SAE Technical Paper No. 932512, 1993.
21 J. Klapp, L. Sigalotti, and E. D. L. C. Sanchez, in *ASME 2008 International Mechanical Engineering Congress and Exposition*, Boston, USA, 31 October-6 November 2008, paper No. IMECE2008-67673, pp. 631-640.
22 J. Bohbot, Y. Blacodon, and B. Scheurer, "Aerodynamic flow simulation in an internal combustion engine using the smoothed particle hydrodynamics method", SAE Technical Paper No. 2011-24-0029, 2011.
23 A. A. Shabana, and R. Y. Yakoub, J. Mech. Des. **123**, 606 (2001).
24 R. Y. Yakoub, and A. A. Shabana, J. Mech. Des. **123**, 614 (2001).
25 A. M. Mikkola, and A. A. Shabana, Multibody Syst. Dyn. **9**, 283 (2003).
26 Q. Tian, Y. Q. Zhang, L. P. Chen, and J. J. Yang, Nonlinear Dyn. **60**, 489 (2010).
27 Q. Tian, C. Liu, M. Machado, and P. Flores, Nonlinear Dyn. **64**, 25 (2011).
28 C. Liu, Q. Tian, and H. Y. Hu, Multibody Syst. Dyn. **26**, 283 (2011).
29 C. Liu, Q. Tian, D. Yan, and H. Y. Hu, Comput. Methods Appl. Mech. Eng. **258**, 81 (2013).
30 W. Hu, Q. Tian, and H. Y. Hu, Nonlinear Dyn. **75**, 653 (2014).
31 D. Negrut, A. Tasora, H. Mazhar, T. Heyn, and P. Hahn, Multibody Syst. Dyn. **27**, 95 (2012).
32 A. Pazouki, R. Serban, and D. Negrut, Archive Mech. Eng. **61**, 2 (2014).
33 W. Hu, Q. Tian, and H. Y. Hu, Nonlinear Dyn. **84**, 2447 (2016).
34 J. G. de Jalón, and B. Eduardo, *Kinematic and Dynamic Simulation of Multibody Systems: The Real-Time Challenge* (Springer, New York, 1994).
35 J. G. de Jalón, Multibody Syst. Dyn. **18**, 15 (2007).
36 J. J. Monaghan, J. Comput. Phys. **82**, 1 (1989).
37 J. J. Monaghan, J. Comput. Phys. **136**, 298 (1997).
38 A. N. Parshikov, S. A. Medin, I. I. Loukashenko, and V. A. Milekhin, Int. J. Impact Eng. **24**, 779 (2000).
39 A. N. Parshikov, and S. A. Medin, J. Comput. Phys. **180**, 358 (2002).
40 S. H. Cha, and A. P. Whitworth, Mon. Not. R. Astron. Soc. **340**, 73 (2003).
41 W. Benz, *Smooth Particle Hydrodynamics: A Review. The Numerical Modelling of Nonlinear Stellar Pulsations* (Springer, Netherlands, 1990), pp. 269-288.
42 J. Gerstmayr, and A. A. Shabana, Nonlinear Dyn. **45**, 109 (2006).
43 O. N. Dmitrochenko, and D. Y. Pogorelov, Multibody Syst. Dyn. **10**, 17 (2003).
44 O. Dmitrochenko, and A. Mikkola, J. Comput. Nonlinear Dyn. **3**, 041012 (2008).
45 A. A. Shabana, *Computational Dynamics*, 3rd ed. (Wiley, New York, 2010).
46 Q. Tian, L. P. Chen, Y. Q. Zhang, and J. Yang, J. Comput. Nonlinear Dyn. **4**, 021009 (2009).
47 B. Hussein, D. Negrut, and A. A. Shabana, Nonlinear Dyn. **54**, 283 (2008).
48 A. A. Shabana, and B. A. Hussein, J. Sound Vib. **327**, 557 (2009).
49 B. A. Hussein, and A. A. Shabana, Nonlinear Dyn. **65**, 369 (2011).
50 J. Chung, and G. M. Hulbert, J. Appl. Mech. **60**, 371 (1993).
51 M. Arnold, and O. Brüls, Multibody Syst. Dyn. **18**, 185 (2007).
52 Q. Tian, Y. L. Sun, C. Liu, H. Hu, and P. Flores, Comput. Struct. **114-115**, 106 (2013).
53 C. Liu, Q. Tian, and H. Y. Hu, Mech. Mach. Theor. **52**, 106 (2012).
54 J. J. Monaghan, J. Comput. Phys. **110**, 399 (1994).
55 M. Hermanns, *Parallel Programming in Fortran 95 Using OpenMP* (Universidad Politecnica de Madrid, Spain, 2002).
56 J. J. Monaghan, and A. Kos, J. Waterw. Port Coast. **125**, 145 (1999).
57 J. H. Seo, I. H. Jung, T. W. Park, and J. B. Chai, JSME Int. J. C-Mech. Sy. **48**, 224 (2005).
58 J. Zhao, Q. Tian, and H. Y. Hu, Acta Mech. Sin. **29**, 132 (2013).